2D Phase-Based RFID Localization for On-Site Landslide Monitoring

Arthur Charléty, Mathieu Le Breton, Eric Larose, Laurent Baillet

MDPI

Article

2D Phase-based RFID localization for on-site landslide monitoring

Arthur Charléty *[1], Mathieu Le Breton [2], Eric Larose[1] and Laurent Baillet[1]

[1] Univ. Grenoble Alpes, Univ. Savoie Mont Blanc, CNRS, IRD, Univ. Gustave Eiffel, ISTerre, 38000 Grenoble, France
[2] Géolithe, 38920 Crolles, France
* Correspondence : arthur.charlety@univ-grenoble-alpes.fr

Abstract: Passive Radio-Frequency Identification (RFID), used recently to monitor landslide displacement at a high spatio-temporal resolution, was used to measure only 1D displacement. This study demonstrates the ability to track 2D displacements, using an array of antennas connected to an RFID interrogator. Ten tags were deployed on a landslide for 12 months and 2D relative localization was performed using a Phase-of-Arrival approach. A period of landslide activity was monitored through RFID, and displacements were confirmed by reference measurements. The tags show displacements up to 1.2m over the monitored period. The centimeter-scale accuracy of the technique was confirmed experimentally and theoretically for horizontal localization, by developing a measurement model that includes antenna and tag positions, as well as multipath interference. This study confirms that 2D landslide displacement tracking with RFID is feasible at relatively low instrumental and maintenance cost.

Keywords: Phase localization, landslides, RFID, remote sensing, wireless sensor network, early warning

Key Contribution: Landslide deformations are monitored in 2D through RFID phase measurements ; A 2D sensitivity model allows optimizing antenna position with respect to a set of tags ; Centimetric precision over long time periods is validated experimentally and theoretically

Citation: Charlety, A. ; Le Breton, M.; Larose, E. ; Baillet, L. ; Helmstetter, A. 2D Phase-based RFID localization for on-site landslide monitoring. *Remote Sens.* **2022**, *1*, 0. https://doi.org/

Received:
Accepted:
Published:

1. Introduction

Ground deformation monitoring with a high resolution both in space and time remains a challenge due to the high cost of existing solutions, and to environmental limitations such as meteorological phenomena, rough terrain or dense vegetation. Amongst several remote sensing methods [1,2], surface monitoring of large landslides can be typically performed through Interferometric Synthetic Aperture Radar (InSAR), either by space-borne measurements [3,4] or using ground-based stations [5–9]. Despite the high space resolution of these methods, the station cost remains high and the time resolution can be of multiple days in the case of satellite remote sensing. More localized techniques such as GPS [10–13] and radiofrequency-transponders [14,15] show higher time resolution, but also require on-board power sources which greatly increase initial cost and maintenance.
In this context, Radio-Frequency Identification (RFID) is showing an increasing potential for earth sciences [16,17]. Amongst other applications, it is foreseen as a promising alternative for landslide and civil engineering structures deformation monitoring [18] thanks to its low cost relative to other solutions, and because it works under rain, snow and vegetation [19,20]. It can thus be used as a tool for landslide early-warning [21], forecasting or long-term monitoring [22]. A wide range of solutions exist for tag localization using RFID [23,24], with various possibilities both in the measured quantity and in the measuring scheme.

The quantities most notably used for localization are the Received Signal Strength and the back-scattered phase of arrival. Signal-Strength based methods have been widely used for tag localization [25,26,26–29]. Yet, phase-based methods have shown better precision and reliability in recent years [30–32], notably because they are less sensitive to environmental variations and because the phase of the signal varies more rapidly with distance than the received signal strength.

Phase-based localization is separated in multiple schemes, which are extensively presented elsewhere [33–36]. These schemes generally rely on either multistatic stationary antennas and different carrier frequencies [30,37,38], or on a moving antenna with a known trajectory (Synthetic Aperture Radar technique) [39–43]. This paper will focus on a monostatic multi-antenna Time-Domain Phase Difference (TD-PD) inspired scheme, as TD-PD showed the best results for measuring relative displacements outdoors [18], with a precision of about 1 cm over long time periods for 1D displacement tracking. As of now, RFID systems deployed to monitor moving ground only provide one-dimensional distance information and are subject to phase unwrapping issues that could be solved by using multiple antennas. In this article, we will test the stationary configuration for 2D RFID tag localization using a set of four antennas in a TD-PD relative localization approach, and will also discuss on 3D localization perspectives. To the best of our knowledge, this is the first attempt at 2D-localizing RFID tags in an outdoor scenario, using a monostatic monofrequency multi-antenna setup.

In the following section, we present the instrumentation of the experimental site and the methodology for data acquisition and processing. Section 3 provides a theoretical background and experimental validation of the RFID measurement error, in order to decide on ideal antenna positioning by optimizing the localization accuracy and phase ambiguity. Section 4 reports on an example of 12 months of surface deformation monitoring on the slow moving Harmalière landslide.

2. Instrumentation and Methods

2.1. Experimental Site: Harmalière landslide

The Harmalière landslide (Sinard, Isère, France) is located in the Trièves area about 50 km South of Grenoble in the western Pre-alps (see Figure 1). Trièves appears as a sedimentary plateau eroded by the Drac river, the plateau is formed by Quaternary varved clays and alluvial materials deposited in a glacially dammed lake during the Würm period

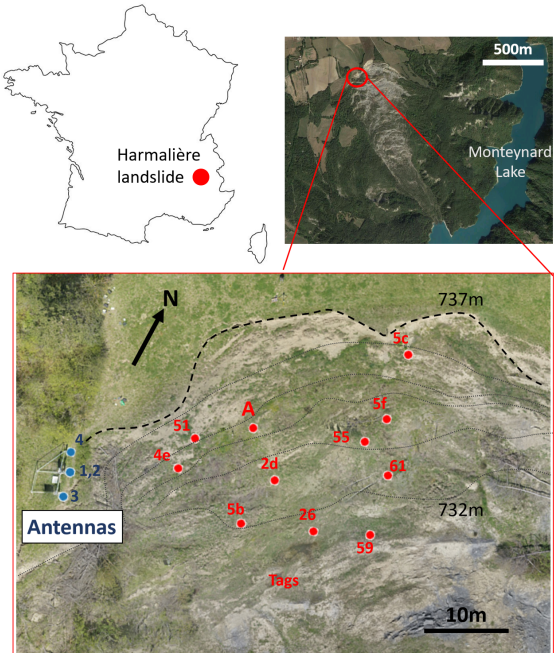

Figure 1. (Top) The Harmalière landslide location in France. (Bottom) Overview of the Harmalière landslide, with the RFID tags distribution (red points). Blue points : antennas and acquisition system. The dotted black line represents the landslide scar, the gray dotted lines represent 1-meter isolines.

[44]. Quaternary sediments also include silts, with sometimes a morainic cover, and rest on either interglacial Riss–Würm period glaciofluvial materials (gravels and sands) or on the underlying Jurassic carbonate bedrock. The thickness of the clay deposits can vary from 0 to a maximum of 200 m [45]. The landslide is southeast oriented, 400 m wide at the top narrowing to 150 m at the toe. It develops from an altitude of 735 m (asl), down to the Monteynard Lake (480 m), over a distance of about 1.5 km. It was abruptly activated in 1981 and has remained active ever since, with new peaks of activity in 2016 and 2017 [46]. The slow moving landslide shows a regressive behaviour, the headscarp retreating at an average velocity of 1 m/year, with very strong variations from year to year (including almost a decade of rest). The central body of the landslide is moving at velocities ranging from cm/year to m/year, with possible dramatic acceleration phases (m/day). A variety of research subjects are currently investigated through it [46,47].

2.2. RFID Instrumentation and localization

2.2.1. RFID Instrumentation

In february 2020, a portion of the landslide was equipped with a RFID system consisting of 32 battery-assisted passive tags and an acquisition station located near the landslide scar (see Figure 1). These tags can last about a decade without maintenance or replacement, in the present real-time monitoring scenario. The station includes 4 antennas, an interrogator (Impinj SR420), a micro-computer (RPI-3B), and a modem to send the data automatically to a remote server, as described by (patent pending FR-17/53739). It is powered by a photovoltaic module and a wind turbine. The station collects RFID data during 3 minutes every 20 minutes from every tag and every antenna. The data includes the Phase of Arrival (that we will call phase) measured at 865.7 Hz, the Received Signal Strength Indication and the tag temperature. The tags were placed by pairs on fiber glass stakes, respectively 50 cm and 1 m above ground. They are spread out within the antennas reading range in a zone approximately 30m x 30m wide (see Figure 1), in such a way as to maximize the line-of-sight readability of each tag by multiple antennas. To validate the RFID localization calculations, the position of the tags was measured with a LEICA TCR805

tacheometer and a handheld target (estimated precision 4 cm), approximately once every month.

2.2.2. RFID Localization Scheme

TD-PD is a relative ranging technique based on a phase variation $\delta\phi = \phi_1 - \phi_0$ between two measurements at different points in time. $\delta\phi$ is related to the radial distance variation $\delta r = r_1 - r_0$ between tag and reader antenna, by the following equation:

$$\delta r = -\frac{c}{4\pi f}\delta\phi \tag{1}$$

where f is the frequency of the electromagnetic wave (see values above) and c is the speed of light in the propagation medium. It is important to note that Eq. 1 is only valid for displacements smaller than $\lambda/4 \approx 8cm$ between two phase measurements because of phase ambiguity. In the present case this condition is generally fulfilled as the incremental displacements are small compared to the wavelength (usually less than 1 cm between two successive acquisitions). Moreover, a series of phase measurements can generally be unwrapped using well-defined algorithms. In that case, Equation 1 is valid for any unwrapped phase variation.
Section 3 will present a multidimensional localization scheme based on TD-PD.

3. Theoretical model

In this section we derive a mathematical model for phase-based RFID localization, in order to compute the localization error of our real experiment. The main goal of this derivation is to study the origins of the localization uncertainty, mainly with regard to the system geometry and the physical measurement process.
From now we will consider that all phase measurements are unwrapped, and that Equation 1 is valid for all phase variations. Most presented tags were correctly read and no unwrapping error was detected on the monitored period. The specific case of an unwrapping error is to be studied separately, and does not fit in the scope of this work.
In the following, index i will describe a series of measurements starting at $i = 0$ and j will describe the antenna indexing.

3.1. Localization model

3.1.1. One dimensional TD-PD

The localization method presented in this paper is based on the tag phase shift measured by each antenna, at different points in time (TD-PD)[36]. In a homogeneous medium, the phase shift $\phi_{i,j} - \phi_{0,j}$ between the initial and the i-th (unwrapped) phase measurement, is directly proportional to the radial displacement $\delta r_{i,j}$ between the tag and antenna j (see Eq. 1).

Assuming an initial radial distance $r_{0,j}$, we get a series of radial distances $r_{i,j}$ from a measured phase series $\phi_{i,j}$:

$$r_{i,j} = r_{0,j} + \delta r_{i,j} \tag{2}$$

where $\delta r_{i,j}$ is obtained directly through Eq. 1. This localization method is hence relative to the initial position, as it doesn't allow for absolute positioning without further information about the system (e.g. when $r_{0,j}$ is not known).

3.1.2. 2D relative displacement approach

Using the measurements of multiple antennas, we can expand this TD-PD method with spatial considerations. For this purpose we need both the phase measurements and geometrical coordinates (x_j, y_j) of each antenna. This derivation focuses on the 2D problem,

and the 3D case will be shortly discussed at the end.
We define the initial distance $r_{0,j}$ from the antenna j to the tag:

$$r_{0,j} = \sqrt{(x_j - x_0)^2 + (y_j - y_0)^2}$$

where (x_0, y_0) are the initial coordinates of the tag and (x_j, y_j) those of the antenna. Thanks to Eq. 2 we obtain a series of radial displacements from the phase measurements of each antenna. From these radial distance measurements, a multilateration approach [48] can be applied to estimate the most probable position $(\hat{x}_i, \hat{y}_i)$ for the tag at the i^{th} position. Amongst various possible methods of multilateration, we used an optimization algorithm that minimizes the following cost function Cf for the i-th measurement:

$$Cf_i(x,y) = \sum_{j=1}^{N_a} \left| r_{i,j} - \sqrt{(x_j - x)^2 + (y_j - y)^2} \right| \tag{3}$$

$$(\hat{x}_i, \hat{y}_i) = \underset{(x,y)\in\mathbb{R}^2}{argmin}\left(Cf_i(x,y)\right)$$

where (x, y) are the test point coordinates, N_a is the number of antennas, $r_{i,j}$ is the i-th radial distance from antenna j, and $(\hat{x}_i, \hat{y}_i)$ is the most probable tag position. The minimization of this cost function was performed using the Trust-region optimization algorithm [49] implemented in the Scipy-optimize Python module.

3.2. Geometrical localization sensitivity

In this section we focus on theoretical considerations regarding the localization sensitivity of the geometrical antenna-tag system, in order to compute the value and direction of a displacement error of the tag, with respect to a phase measurement error [19]. For a given antenna position (x_j, y_j) , the absolute phase accumulated on a linear ray path (line of sight, LOS) between the antenna and a point (x, y) is expressed as follows:

$$\phi_j(x,y) = -\frac{4\pi f}{c} \times \sqrt{(x_j - x)^2 + (y_j - y)^2}$$

Let us define $K_{\phi j}$ as the space gradient of the measured phase ϕ_j, also defined as the phase sensitivity kernel, expressed in spatial dimension as:

$$K_{\phi j}(x,y) = \begin{bmatrix} \frac{\partial \phi_j}{\partial x} \\ \frac{\partial \phi_j}{\partial y} \end{bmatrix} = \begin{bmatrix} K^x_{\phi j} \\ K^y_{\phi j} \end{bmatrix} \tag{4}$$

For a system consisting of two antennas (A and B) and small phase variations, the relation between the phase variation vector $\delta\phi$ and the true tag displacement δr can then be approximated by the linear matrix system:

$$\begin{bmatrix} \delta\phi_A \\ \delta\phi_B \end{bmatrix} = \begin{bmatrix} K^x_{\phi_A} & K^y_{\phi_A} \\ K^x_{\phi_B} & K^y_{\phi_B} \end{bmatrix} \begin{bmatrix} \delta x \\ \delta y \end{bmatrix}$$

That we can simply rewrite :

$$\delta\phi = K\delta r \tag{5}$$

Equation 5 holds for any number of phase measurements (thus any number of antennas N_a), and any number of space dimensions M ; in such cases K will be an $M \times N_a$ matrix.

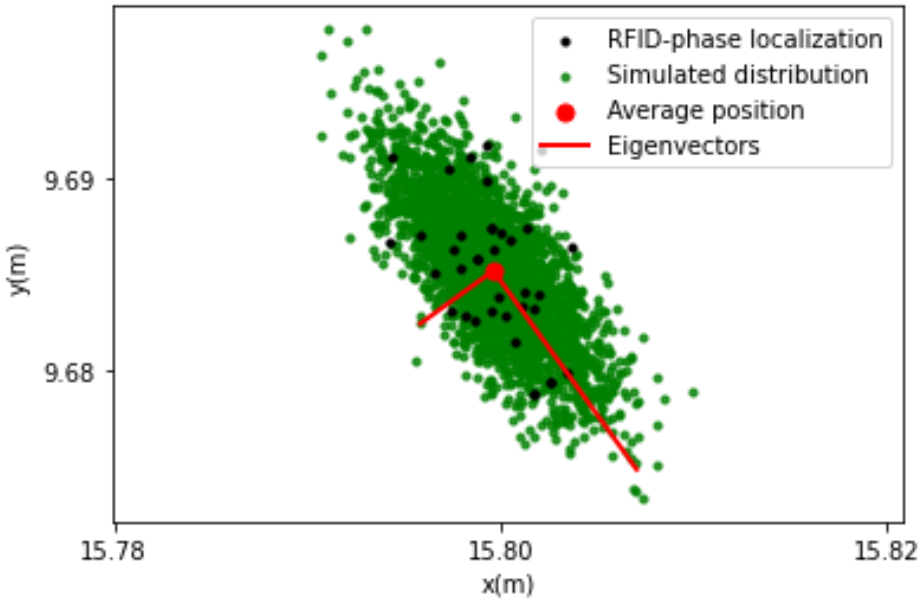

Figure 2. Localization error shape at the position of tag A (see Fig.1) compared with the RFID position estimation during a stable period in l'Harmalière (November to December 2020). The green point distribution is computed through the K^{-1} transformation (see Eq. 6), using a Gaussian phase distribution with a standard deviation of 0.04 rad. The eigenvectors of the green distribution (red lines) are scaled up to encompass 97% of the data. The black points correspond to the RFID-Phase localization results. The antennas positions are set as in the real experiment (see Fig.1).

It expresses the direct solution of the phase-based relative localization problem, where K represents the transformation matrix from measured phase space to localization space. For the sake of simplicity, consider now that $N_a = M = 2$, which implies a bijective relationship between phase measurements and tag 2D relative displacement. In this case the invertibility of the K matrix is almost always possible : the only exceptions are when the point position (x, y) coincides with that of one antenna, or when it is aligned with the two antennas. We exclude these limit cases that have no significance in our experiments. The above equation can then be reversed and gives the theoretical phase sensitivity of the tag position:

$$\delta r = K^{-1}\,\delta\phi \tag{6}$$

We now consider the linear transformation matrix K^{-1} on which we will apply Singular Value Decomposition (SVD). Any real matrix can be decomposed as follows [50]:

$$K^{-1} = U\Sigma V^{\top} \tag{7}$$

In our model $V^{\top}$ represents the eigenvectors in phase space, Σ the diagonal eigenvalue matrix and U the eigenvectors in localization space.

In this derivation, we assume the same variance for all phase measurements, hence the covariance matrix C_ϕ is defined as follows :

$$C_\phi = \sigma_\phi^2 \cdot I_{N_a} \tag{8}$$

where σ_ϕ is the typical phase standard deviation and I_{N_a} is an identity matrix of size N_a. C_ϕ is thus a constant diagonal matrix in our model, with typical values of 0.04 rad. This phase standard deviation is both an experimentally computed value and also corresponds to the modeled approximation of Equation 12 (see next section).

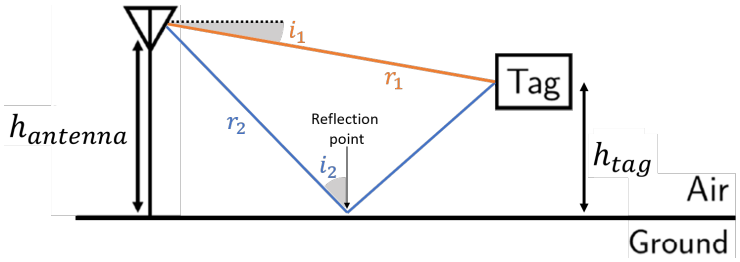

Figure 3. Schematic definition of the two-ray multipath model. The orange line represents the Line of Sight path with angle i_1 and propagation distance r_1. The blue line represents the reflected path with angle i_2 and propagation distance r_2. h_{tag} and $h_{antenna}$ are the tag and antenna heights above ground.

Considering a given phase measurement uncertainty for each antenna, we can plug any phase distribution into the transformation from Eq.7. The shape and orientation of the resulting spatial distribution around tag position (that we will call localization spot) is described by the localization-space covariance matrix C_r. This matrix can be expressed in the following way, depending on K^{-1} as well as the hypothetical covariance of the phase measurement matrix C_ϕ:

$$C_r = (K^{-1})^\top C_\phi K^{-1} = U\Sigma^2 U^\top \tag{9}$$

Extracting the eigenvalues and eigenvectors of C_r allows for a completely analytical determination of the localization spot properties (especially the direction of highest error), for a given antenna-tag geometry, as shown in Fig. 2. With a phase error of 0.04 rad and at the given tag position, we expect a localization random error of about 1 cm. Note that in the model, any relative increase in phase error will result in the same relative increase in localization error, as the measurement operator is linear.

The calculation presented above can be extended to a 3 antennas system for a 3D localization problem, following Equations 1 to 9 with K a 3×3 matrix. In the case where $N_a > 3$, the system from Eq. 5 is overdetermined, and a least-squares solution has to be found [51] [52]. Using the pseudo-inverse of K, Equation 6 then gives:

$$\delta r = (K^\top K)^{-1} K^\top \delta\phi \tag{10}$$

This new system can be solved and the eigenvectors computed by considering the transformation matrix $(K^\top K)^{-1}K^\top$.

3.3. Phase error model : multipath, phase standard deviation and radiation pattern

While the previous section focuses on geometrical localization error, we will now incorporate the impact of real-scenario error sources, e.g. antenna radiation pattern and multipath. The following derivation is based on the work of [20].

3.3.1. Multipath propagation model

Multipath interference is a major challenge in RFID-localization and several solutions have been proposed to estimate, reduce or mitigate its effect on measurements [53,54]. To start investigating multipath we use a simple two-ray model, assuming that the measured signal is a superposition of the line of sight ($p = 1$) signal and a signal reflected on the ground ($p = 2$), as shown in Figure 3. The two signals propagate over different path lengths r_p and orientations, which translate in different received power values due to Friis law:

$$P_p(r) = \left(\frac{\lambda}{4\pi r_p}\right)^2 \times P_t \cdot G_T(i_p) \cdot G_R(i_p) \quad for \;\; p = \{1,2\}$$

where P_t is the power transmitted by the antenna, P_p is the received power along path p, G_r and G_t are the receiver and transmitter gain which depend on the signal orientation angle i_p and the antenna radiation pattern, λ is the carrier wavelength and r_p is the path propagation distance. We can then define the amplitude gain $A_p(i_p, r_p)$ for the Line Of Sight (1) and reflected (2) signals :

$$A_1(i_1, r_1) = \frac{1}{r_1}\sqrt{G_t(i_1) \cdot G_r(i_1)}$$

$$A_2(i_2, r_2) = \frac{1}{r_2}R(i_2)\sqrt{G_t(i_2) \cdot G_r(i_2)}$$

where $R(i_2)$ is the reflection coefficient impacting the reflected ray (which depends on ground relative permittivity). The received signal voltage s_p after normalization by the initial emitted voltage, can be expressed by the following phasor:

$$s_p(i_p, r_p) = A_p(i_p, r_p) \cdot \frac{\lambda}{4\pi} \cdot e^{-jkr_p} \quad for \ p = \{1, 2\} \tag{11}$$

where k is the wave number. The resulting signal s_{tot} arriving on the tag is the sum of the two phasors:

$$s_{tot} = s_1(i_1, r_1) + s_2(i_2, r_2)$$

After accounting for tag modulation efficiency L_t [55] and due to the reciprocity of all gain values during the backscattered propagation, the full signal phasor received by the station antenna is finally expressed as follows:

$$s_{full} = s_{tot}^2 \cdot L_t$$

As a reminder, the squared s_{tot} corresponds to the back-and-forth path of the signal.

3.3.2. Two types of phase error

We define the phase measurement error as the difference between the ideal LOS phase and the full received phase. This error can be divided in two contributions: the phase random deviation σ_{rdm} and the systematic phase bias ϕ_b, which are both consequences of multipath interference. Let us now consider these two error contributions separately.

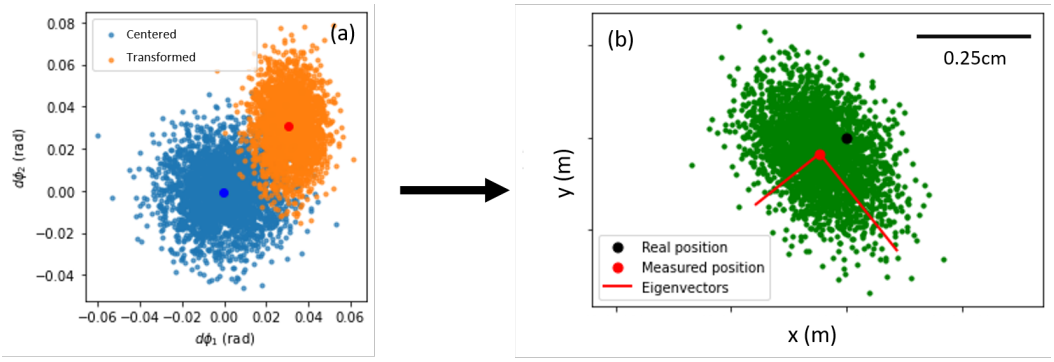

Figure 4. Schematic description of the matrix transformations in phase space towards real 2D space for a 2-antennas system. (a) Representation of the simulated multipath-induced phase measurement distribution (orange) compared to the previously assumed centered distribution (blue), highlighting the scaling S and translation T. The translation is illustrated by the shift between the center of the blue distribution and the center of the red distribution. (b) True space localization spot obtained by further transformation via the K^{-1} matrix. The antennas are not represented. The systematic bias is again illustrated by the shift between the real position (black point) and the center of the measured distribution (red point).

Previous works [18] have shown a direct relationship between antenna received power P(W) and phase random deviation σ_{rdm}(rad), using the same acquisition configuration (tag, interrogator, and communication protocol):

$$\sigma_{rdm} = \frac{4\pi f}{c} \cdot 9.5 \cdot 10^{-9} / \sqrt{P} \tag{12}$$

where c is the light velocity and f the carrier frequency. This empirical relationship reproduces the phase error value of 0.04 rad used in the previous section. The received power greatly depends on propagation distance but also on multipath interference, which is why σ_{rdm} is multipath-sensitive.

The systematic phase bias ϕ_b will be defined as the difference between the ideal LOS phase ϕ_1 and the full received phase ϕ_{full}:

$$\phi_b = arg(s_1^2) - arg(s_{full}) = \phi_1 - \phi_{full} \tag{13}$$

The phase bias obviously depends on multipath behaviour. In phase space, the two error contributions σ_{rdm} and ϕ_b can be interpreted respectively as a scaling and translation operation on an ideal phase measurement distribution. Indeed, σ_{rdm} represents the width of the measurement error distribution, and the bias ϕ_b represents the center of this distribution : compared to the LOS ideal measurement, the true measurement will thus be translated by ϕ_b and scaled to a width of σ_{rdm}. Assuming a gaussian behaviour for the measurement process, each antenna j will hence present a measurement distribution ϕ_j following a normal law :

$$\phi_j = \mathcal{N}(\phi_b, \sigma_{rdm}^2)$$

These considerations can be applied in the phase-localization scheme presented in the previous section, via a multi-antenna phase distribution.

Let us define the scaling matrix S and the translation vector T as follows:

$$S = \begin{bmatrix} \sigma_1 & 0 \\ 0 & \sigma_2 \end{bmatrix}$$

$$T = \begin{bmatrix} \phi_{b1} & \phi_{b2} \end{bmatrix}^\top$$

The entries of S originate from Eq. 12 and the entries of T from Eq. 13. They correspond to the values of phase random error and phase bias measured by each antenna (N_a=2 in this simple scenario). Note that the phase random deviation values σ_j are different for each antenna because of geometrical reasons : each antenna is in a different location, hence the multipath and radiation patterns do not yield the same error values. The scaling S in phase space allows for a definition of the phase covariance matrix C_ϕ :

$$C_\phi = S \cdot S^\top$$

C_ϕ can be used in the Singular Value Decomposition to compute the displacement error eigenvectors via the displacement covariance matrix C_r (see Equation 9). The localization spot dimensions are hence fully described by the following covariance matrix in displacement space C_r :

$$C_r = (K^{-1})^\top C_\phi K^{-1} \tag{14}$$

On the other hand, the translation T induced by the phase bias corresponds to a translation dr_b in displacement space, obtained by :

$$dr_b = K^{-1} \cdot T \tag{15}$$

Equations 14 and 15 represents our best attempt to model the deviation from an ideal LOS phase measurement, taking into account the various phase measurement errors, and the geometry of the system. Figure 4 presents a 2D schematic view of the measurement distributions from phase space to displacement space. We see that the phase distribution is scaled and translated in phase space, compared to the centered distribution that was set in Equation 8. In displacement space this gives a specific localization spot with covariance C_r, translated from the true LOS measurement by vector dr_b. The specific values of C_r and dr_b will be discussed in section 4.2.

4. Harmalière Landslide monitoring

In this section we will discuss the specific case of the Harmalière landslide RFID system. After presenting the acquired data, the theoretical model will be applied to the real system geometry, then the localization results will be presented

4.1. Real phase data

4.1.1. Available RFID Data

Among the 32 tags installed in the field, 10 were read almost continuously by more than two antennas for 12 months (January 2021 - February 2022). The rest of the tags yielded partial results that could not be used for 2D localization via the present scheme. Two main factors can explain the lack of readability of some tags, namely the narrow horizontal directivity of the antennas (+/- 30° aperture) and signal attenuation: the furthest tags showed the lowest signal quality. Generally speaking, the tags placed 50 cm above ground showed worse results than those placed 1 m above ground, both in terms of data quality and localization accuracy. This observation corresponds to the above theoretical results (see Section 4.2 and Figure 7-c), which tend to show that displacements close to the ground are subject to stronger multipath interference. This study will only show the tags read by at least two antennas during the whole period.
The unwrapped phase measured during the January 2021 - February 2022 time period is presented in Fig. 5 for tag A. The data (70 measurements per day) was averaged over 24h periods before applying the localization algorithm, in order to mitigate the daily phase variations due to humidity and temperature. The missing values correspond to strong weather events that most likely depleted the battery of the acquisition system, or to hardware failures.

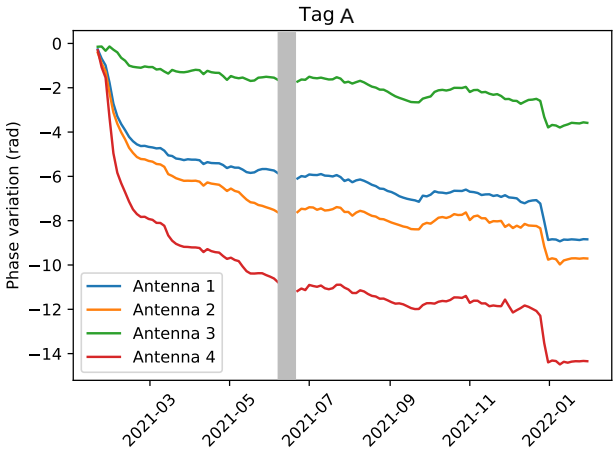

Figure 5. Unwrapped phase variation for tag A, measured by 4 antennas at a frequency f=865 MHz, from January 2021 to February 2022. The grey bar shows a period of missing data due to hardware failure. Data was directly available after replacement of the malfunctioning device.

4.2. Application of the model to a real geometry

Before presenting the localization results, we will first apply the previously developed model to the real system geometry. The workflow is presented in Figure 6, showing how the real parameters come together with the geometry and model to compute the localization error mapping.

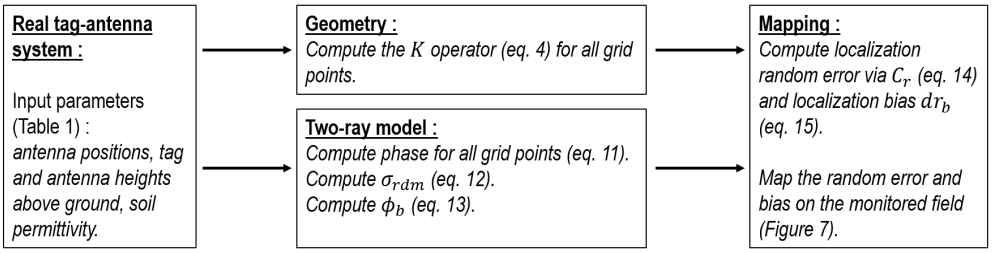

Figure 6. Schematic view of the workflow used in order to estimate the localization error and bias in the real-scenario Harmalière geometry.

We have set the model geometry according to Table 1, which corresponds to the Harmalière setup geometry. The number of antennas is now set to $N_a = 4$. The ground relative permittivity is set according to the literature for dry soils [56,57], and the following results correspond to this dry soil scenario. In the case of a wet soil, we expect the relative permittivity to reach values around 25. In the model, this turned out to generally increase the phase error (and localization error) values by about 30%, which can represent millimeters to centimeter values depending on the context (see Section 4.2.2).

Antenna no.	x (m)	y (m)	z (m)
1	0	0	0
2	0.018	-0.034	1.55
3	0.013	-2.608	0.256
4	-0.338	2.148	0.287

$h_{antenna}$ (m)	3
h_{tag} (m)	1
Ground relative permittivity	2.4

Table 1. (Up) Geometrical parameters for the positions of the four antennas in the Harmalière setup. (Down) Values of the main variables used in the two-ray model (see Figure 3); the height of the station is relative to the ground at the same position.

4.2.1. Random localization error of the experimental field

The previous developments (Eqs. 14-15) have been applied to the geometry installed in the Harmalière landslide, as shown in Figure 7. A mapping of the random localization error (related to σ_{rdm}, Eq. 12) is shown in Fig. 7a. We see that the lowest error is obtained when facing the antennas, which are oriented east-ward. The plot is separated in two main areas, discriminated by the 2 cm random localization error value. This value was chosen because it reflects the target precision in our application.

4.2.2. Systematic localization bias of the experimental field

The systematic localization bias (related to ϕ_b, Eq. 13) presented in Fig. 7b-c is not to be understood as a raw localization error, but as a varying bias when moving in space: the interference between LOS and reflected signal changes with tag position.

In order to better understand the effect of the multipath-induced phase bias on 3D displacement measurements, we propose to consider the typical case of a 1 m displacement along a given spatial direction, starting from the position of tag A. The symmetry of our experiment being mainly cylindrical, we consider a cylindrical coordinate system with its central axis in ($x = 0$, $y = 0$). For this displacement we compute the localization bias

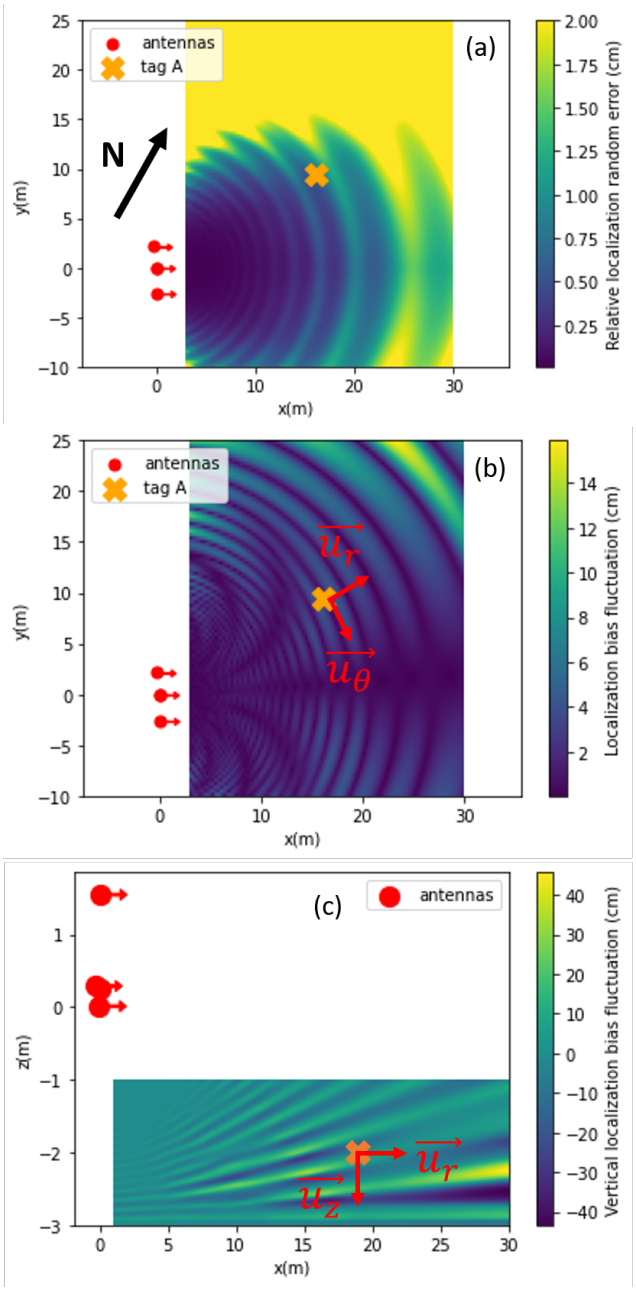

Figure 7. Mapping of the 2D localization error extracted from Eqs. 14 and 15, simulating the geometry of l'Harmalière setup. The red dots represent the reader antennas, and the arrows show the principal antenna directions. The orange cross indicates the position of tag A. The vectors $(\vec{u_r}, \vec{u_\theta}, \vec{u_z})$ define the cylindrical coordinate system used later on. (a) The colormap shows the random localization error (maximum dimension of the localization spot) up to 2 cm, related to the phase random deviation σ_{rdm}. The localization bias is not shown. (b) Color-mapping of the systematic localization bias (related to ϕ_b) in the xOy plane, that shows oscillations with meter-order spatial frequency and increasing amplitude with distance from the measurement system. The random localization error is not shown. (c) Color-mapping of the systematic localization bias in the xOz plane, with higher oscillation amplitude and frequency. The ground is located at z=-3 m.

Bias \ Dir.	$\vec{u}_\theta$	$\vec{u}_r$	$\vec{u}_z$
max. $\vec{u}_\theta$ bias	<1cm	<1cm (*1cm*)	10cm (*20cm*)
max. $\vec{u}_r$ bias	1cm	1cm (*1cm*)	2cm (*15cm*)
max. $\vec{u}_z$ bias	1cm	<1cm (*5cm*)	70cm (*110cm*)

Table 2. Direction-dependent localization bias in the 3 directions (cylindrical coordinates), for a typical 1 m displacement. Each column corresponds to a different direction of displacement. Each line represents the localization bias amplitude along a certain direction, during the 1 m displacement. The *values in italic* correspond to field experiment localization bias measurements.

fluctuation, and project it on every space direction (along $\vec{u}_\theta$, $\vec{u}_r$, $\vec{u}_z$) in order to obtain an amplitude value. The displacement length of 1 m was chosen both because it encompasses about one phase bias cycle, and because it corresponds to the actual displacement we measured in the real landslide scenario (see next section).
Table 2 reports the simulated localization bias amplitude in the three space directions, together with real error measurements that were performed on field.

- The direction that produces the least bias variation is a $\vec{u}_\theta$ displacement, which corresponds to the quasi rotational symmetry of the system.
- A horizontal displacement along $\vec{u}_r$ yields a small localization error. This confirms previous studies and demonstrates a centimeter precision for the RFID technique in the horizontal plane [18].
- A vertical displacement along $\vec{u}_z$ undergoes several strong bias oscillations (Fig. 7c). The subsequent localization error is a cumulative effect of both the strong multipath interference and the small vertical aperture of the measurement system.

These results tend to show that vertical localization in the current localization scheme cannot be performed with precision. The mutlipath effect along with the high system sensitivity in this direction, yield a very high localization bias. This is why we will not present *Oz* localization results in the following section. This model highlights the importance of the geometrical features of the system, such as antenna position and spacing, tag height and direction of displacement.

4.3. Surface displacement monitoring results

In this section, we present the experimental localization of the tags in the Harmalière landslide. We first focus on the 2D localization of one specific tag (tag A) in Figure 1, then we recapitulate on the whole setup and discuss the results.

4.3.1. 2D relative displacement for one tag

The 2D displacement of tag A, computed from the radial displacements using multilateration and data from the four antennas (see Eq. 3), is shown in Fig. 8 against reference tacheometer position measurements. The xOy results are in good agreement with reference points. Note that for stable phase periods (for example July 2021) the localization algorithm yields very stable results with a centimeter scale variability, which is in agreement with the theoretical localization error presented in Fig. 2. This correspondence between theory and experiment during stable periods is observed for several tags, further validating the measurement error model. Note that Figure 2 does not present any phase bias results, but focuses only on measurement random deviation (dimensions of the localization spot).

4.3.2. 2D localization for all tags

Figure 9 shows an overview of the xOy displacement norm measured by RFID-Phase for all available tags during the measurement period. The total displacement is also shown

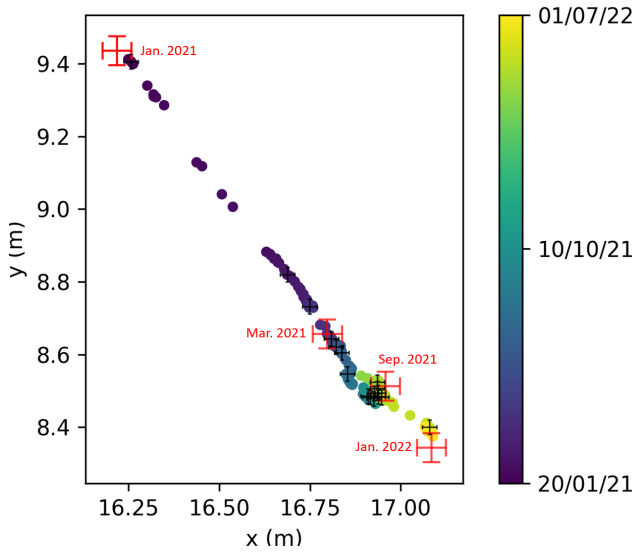

Figure 8. RFID localization in the xOy plane, using phase data for tag A (Figure 5). The total displacement is about 1.6 m. The color plot represents the time evolution of the RFID relative localization. The red crosses represent the reference measurements using tacheometer, with an estimated error of about 4 cm. The tacheometer measurement of March 2021 is set as an absolute reference for relative localization. The black crosses correspond to the estimated random error bars for TD-Phase localization (calculated via the model developped in section 4.2).

for every tag in Table 3. All RFID localization results fit with reference measurements, notably for displacements greater than 1 m. The steep displacement increase in January 2022 concerning tags 51, 4e and A, was confirmed by tacheometer measurement. This rapid and localized deformation generated cracks, and a landslide retrogression of about 2 meters in this area. A south-east tendency is clearly validated and corresponds to the landslide main direction, as can be seen in the qualitative vector mapping in Figure 10, with various displacement amplitudes depending on tag location. This opens the way to 2D spatio-temporal monitoring of the landslide surface, offering the possibility to better understand the physical mechanisms at the origin of the landslide activation and propagation, and to build new early warning monitoring systems.

Tag	51	A	4e	26	55	5f	2d	5c	59	5b
Total disp (m)	1.54	1.37	1.20	0.81	0.75	0.85	0.69	0.67	0.74	0.56
Reference (m)	1.57	1.45	1.28	0.81	0.79	0.74	0.77	0.74	0.72	0.59

Table 3. Total 2D displacement norm for all presented tags computed from RFID phase, from January 2021 to February 2022. The reference is computed from the tacheometry measurements, with an estimated error of $\pm 4cm$.

4.4. Discussion

In this section we briefly discuss some of the results presented in this paper, as well as the future developments for the RFID localization system.

4.5. Localization error and reference measurements

In the context in which RFID localization was performed, absolute reference localization at a centimeter level was a complicated task. For practical reasons, reference positions taken via GPS were not accurate enough to be compared to RFID localization results. This is why tacheometry was used, which is a relative localization method. A landslide is an ever-changing environment, and using absolute references such as trees or antennas involves several sources of error. For this reason, the tacheometer uncertainty given in

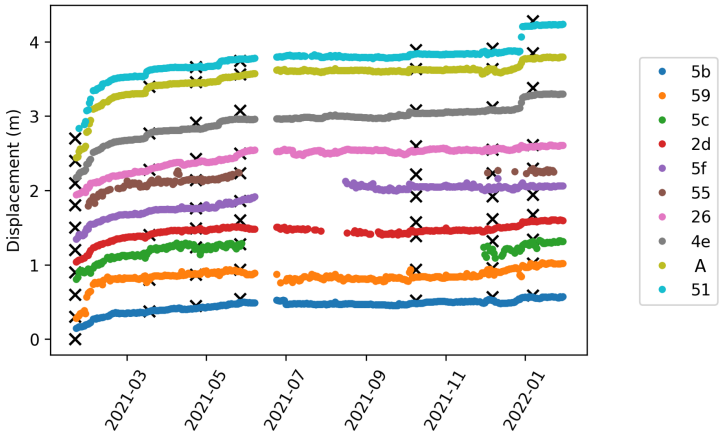

Figure 9. Cumulative 2D displacement norm for each tag, with reference measurements performed via tacheometer (black crosses). An offset was added to every plot, to increase readability. The total displacement values are given in Table 3.

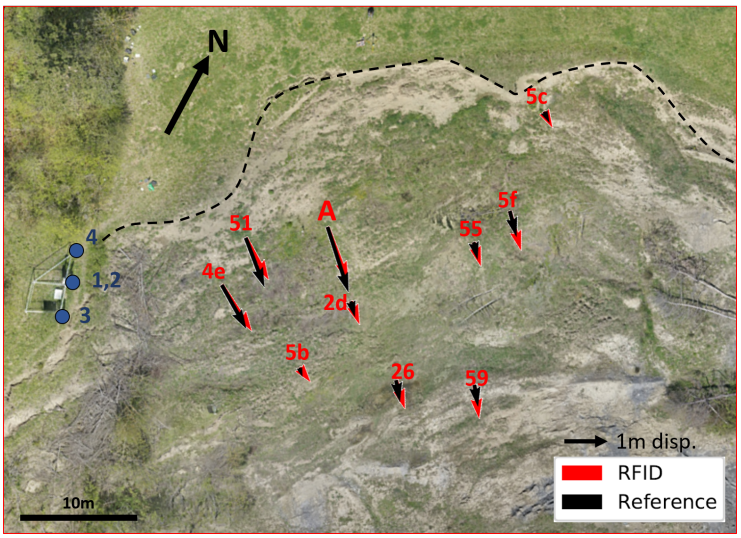

Figure 10. Vector mapping of the total 2D displacement for all available tags, from January 2021 to September 2021. The scale is modified for clarity, with a 1m displacement reference (black arrow). The red arrows represent the displacement estimated from the RFID measurements, and the black arrows represent the displacement computed from reference measurements. The blue points numbered 1 to 4 correspond to the reader antennas.

Table 3 is $\pm 4cm$. As was already mentioned in previous works [18], RFID phase outdoor localization can outperform the reference measurements.

4.5.1. Discussion on antenna position

The above model (Section 4.2) is a tool for optimizing the antenna positions in a given terrain, in order to minimize localization errors originating from both multipath and geometry. We performed calculations for several geometrical cases in a plane xOy geometry, searching for the lowest random deviation in the monitored zone. As a general rule, we conclude that surrounding the field with antennas yields the best accuracy (lowest localization random deviation). For example, if 4 antennas are spread around the Harmalière field, the horizontal random localization error is expected to go down to 1 mm.

Such setups are not always possible in real-environment operational situations : the experimental setup obviously has to be designed taking into account the operational constraints and priorities. In cases where a portion of the field is inaccessible for example,

the distance between antennas (system aperture) should be maximized to obtain the lowest random deviation. This guideline has limitations such as cable length or station cost, hence the final setup will generally be a compromise between precision and station/maintenance cost. Note that other localization methods such as Angle of Arrival Techniques [54,58] rely on different system geometries and will not lead to the same optimal antenna disposition. The guidelines herein provided only apply to a relative displacement scheme, and absolute positioning is a different matter which we do not discuss here.

4.5.2. Perspective for improving data availability

In this work the tags that yielded only partial data (less than 2 antennas readings, long time periods without data) were not used, although more complex data assimilation techniques could be of use [59,60]. Exploiting both the knowledge of the landslide mechanics and the redundancy of information that the system yields, could allow tag monitoring even in partial data scenarios, which are a common issue in outdoor environments. Such techniques will be implemented in future works.

5. Conclusion

We have derived a phase-based 2D localization error theoretical model that allows for error estimation in the scenario of two to four static interrogator antennas, taking into account the specific setup geometry. The model is based on both the sensitivity kernel of the measurement system, and a two-ray propagation model (multipath). Under certain conditions, this model confirms the ability for tracking centimetric ground displacements. The in-plane horizontal measurements demonstrate much better accuracy than out-of-plane vertical measurements, due to the preferential horizontal antenna distribution, and ground-reflection multipath interference.
A set of RFID tags was placed on an active landslide and phase measurements were performed during several months to monitor the tags displacement. Results show a clear south-east displacement of about 1 m in the horizontal plane, over the monitored area. The presented method, inspired by the Time-Difference Phase-difference scheme, has shown very good results to monitor relative displacements in 2D at the centimeter scale. Monitoring of landslides using RFID technology proves to be a viable solution, with a centimeter-scale accuracy over large periods of time. A further step in large scale monitoring could be to deploy a moving antenna (SAR) over greater lengths, and to implement a data assimilation approach in order to increase data availability.

6. Aknowledgements

This work was partially funded by the ANR LABCOM GEO3ILAB and by the Region Auvergne Rhone Alpes RISQID project. This work is part of the "Habitability" LABEX coordinated by OSUG. We acknowledge experimental help from B. Vial, M. Langlais, G. Scheiblin, G. Bièvre from ISTerre.

7. References

1. Scaioni, M.; Longoni, L.; Melillo, V.; Papini, M. Remote sensing for landslide investigations: An overview of recent achievements and perspectives. *Remote Sensing* **2014**, *6*, 9600–9652.
2. Zhao, C.; Lu, Z. Remote sensing of landslides—A review. *Remote Sensing* **2018**, *10*, 279.
3. Colesanti, C.; Wasowski, J. Investigating landslides with space-borne Synthetic Aperture Radar (SAR) interferometry. *Engineering geology* **2006**, *88*, 173–199.
4. Strozzi, T.; Farina, P.; Corsini, A.; Ambrosi, C.; Thüring, M.; Zilger, J.; Wiesmann, A.; Wegmüller, U.; Werner, C. Survey and monitoring of landslide displacements by means of L-band satellite SAR interferometry. *Landslides* **2005**, *2*, 193–201.
5. Wang, Y.; Hong, W.; Zhang, Y.; Lin, Y.; Li, Y.; Bai, Z.; Zhang, Q.; Lv, S.; Liu, H.; Song, Y. Ground-based differential interferometry SAR: A review. *IEEE Geoscience and Remote Sensing Magazine* **2020**, *8*, 43–70.

6. Tarchi, D.; Casagli, N.; Fanti, R.; Leva, D.D.; Luzi, G.; Pasuto, A.; Pieraccini, M.; Silvano, S. Landslide monitoring by using ground-based SAR interferometry: an example of application to the Tessina landslide in Italy. *Engineering geology* **2003**, *68*, 15–30.
7. Monserrat, O.; Crosetto, M.; Luzi, G. A review of ground-based SAR interferometry for deformation measurement. *ISPRS Journal of Photogrammetry and Remote Sensing* **2014**, *93*, 40–48.
8. Helmstetter, A.; Garambois, S. Seismic monitoring of Séchilienne rockslide (French Alps): Analysis of seismic signals and their correlation with rainfalls. *Journal of Geophysical Research: Earth Surface* **2010**, *115*.
9. Aryal, A.; Brooks, B.A.; Reid, M.E.; Bawden, G.W.; Pawlak, G.R. Displacement fields from point cloud data: Application of particle imaging velocimetry to landslide geodesy. *Journal of Geophysical Research: Earth Surface* **2012**, *117*.
10. Benoit, L.; Briole, P.; Martin, O.; Thom, C.; Malet, J.P.; Ulrich, P. Monitoring landslide displacements with the Geocube wireless network of low-cost GPS. *Engineering Geology* **2015**, *195*, 111–121.
11. Li, Y.; Huang, J.; Jiang, S.H.; Huang, F.; Chang, Z. A web-based GPS system for displacement monitoring and failure mechanism analysis of reservoir landslide. *Scientific reports* **2017**, *7*, 1–13.
12. Šegina, E.; Peternel, T.; Urbančič, T.; Realini, E.; Zupan, M.; Jež, J.; Caldera, S.; Gatti, A.; Tagliaferro, G.; Consoli, A.; et al. Monitoring Surface Displacement of a Deep-Seated Landslide by a Low-Cost and near Real-Time GNSS System. *Remote sensing* **2020**, *12*, 3375.
13. Dong, M.; Wu, H.; Hu, H.; Azzam, R.; Zhang, L.; Zheng, Z.; Gong, X. Deformation prediction of unstable slopes based on real-time monitoring and deepar model. *Sensors* **2020**, *21*, 14.
14. Intrieri, E.; Gigli, G.; Gracchi, T.; Nocentini, M.; Lombardi, L.; Mugnai, F.; Frodella, W.; Bertolini, G.; Carnevale, E.; Favalli, M.; et al. Application of an ultra-wide band sensor-free wireless network for ground monitoring. *Engineering Geology* **2018**, *238*, 1–14.
15. Mucchi, L.; Jayousi, S.; Martinelli, A.; Caputo, S.; Intrieri, E.; Gigli, G.; Gracchi, T.; Mugnai, F.; Favalli, M.; Fornaciai, A.; et al. A flexible wireless sensor network based on ultra-wide band technology for ground instability monitoring. *Sensors* **2018**, *18*, 2948.
16. Schneider, J.M.; Turowski, J.M.; Rickenmann, D.; Hegglin, R.; Arrigo, S.; Mao, L.; Kirchner, J.W. Scaling relationships between bed load volumes, transport distances, and stream power in steep mountain channels. *Journal of Geophysical Research: Earth Surface* **2014**, *119*, 533–549.
17. Breton, M.L.; Liébault, F.; Baillet, L.; Charléty, A.; Éric Larose.; Tedjini, S. Dense and longdterm monitoring of Earth surface processes with passive RFID – a review, 2021, [arXiv:physics.ins-det/2112.11965].
18. Le Breton, M.; Baillet, L.; Larose, E.; Rey, E.; Benech, P.; Jongmans, D.; Guyoton, F.; Jaboyedoff, M. Passive radio-frequency identification ranging, a dense and weather-robust technique for landslide displacement monitoring. *Engineering geology* **2019**, *250*, 1–10.
19. Le Breton, M.; Baillet, L.; Larose, E.; Rey, E.; Benech, P.; Jongmans, D.; Guyoton, F. Outdoor uhf rfid: Phase stabilization for real-world applications. *IEEE Journal of Radio Frequency Identification* **2017**, *1*, 279–290.
20. Le Breton, M. Suivi temporel d'un glissement de terrain à l'aide d'étiquettes RFID passives, couplé à l'observation de pluviométrie et de bruit sismique ambiant. PhD thesis, Université Grenoble Alpes (ComUE), 2019.
21. Intrieri, E.; Gigli, G.; Mugnai, F.; Fanti, R.; Casagli, N. Design and implementation of a landslide early warning system. *Engineering Geology* **2012**, *147*, 124–136.
22. Intrieri, E.; Carlà, T.; Gigli, G. Forecasting the time of failure of landslides at slope-scale: A literature review. *Earth-science reviews* **2019**, *193*, 333–349.
23. Balaji, R.; Malathi, R.; Priya, M.; Kannammal, K. A Comprehensive Nomenclature Of RFID Localization. 2020 International Conference on Computer Communication and Informatics (ICCCI). IEEE, 2020, pp. 1–9.
24. Miesen, R.; Ebelt, R.; Kirsch, F.; Schäfer, T.; Li, G.; Wang, H.; Vossiek, M. Where is the tag? *IEEE Microwave Magazine* **2011**, *12*, S49–S63.
25. Ni, L.M.; Liu, Y.; Lau, Y.C.; Patil, A.P. LANDMARC: Indoor location sensing using active RFID. Proceedings of the First IEEE International Conference on Pervasive Computing and Communications, 2003.(PerCom 2003). IEEE, 2003, pp. 407–415.
26. Subedi, S.; Pauls, E.; Zhang, Y.D. Accurate localization and tracking of a passive RFID reader based on RSSI measurements. *IEEE Journal of Radio Frequency Identification* **2017**, *1*, 144–154.
27. Rohmat Rose, N.D.; Low, T.J.; Ahmad, M. 3D trilateration localization using RSSI in indoor environment. *International Journal of Advanced Computer Science and Applications* **2020**, *11*, 385–391.

28. Martinelli, F. A robot localization system combining RSSI and phase shift in UHF-RFID signals. *IEEE Transactions on Control Systems Technology* **2015**, *23*, 1782–1796.
29. Shen, L.; Zhang, Q.; Pang, J.; Xu, H.; Li, P. PRDL: relative localization method of RFID tags via phase and RSSI based on deep learning. *IEEE Access* **2019**, *7*, 20249–20261.
30. Scherhäufl, M.; Pichler, M.; Stelzer, A. UHF RFID localization based on evaluation of backscattered tag signals. *IEEE Transactions on Instrumentation and Measurement* **2015**, *64*, 2889–2899.
31. Wang, Z.; Ye, N.; Malekian, R.; Xiao, F.; Wang, R. TrackT: Accurate tracking of RFID tags with mm-level accuracy using first-order taylor series approximation. *Ad hoc networks* **2016**, *53*, 132–144.
32. Zhou, C.; Griffin, J.D. Accurate phase-based ranging measurements for backscatter RFID tags. *IEEE Antennas and Wireless Propagation Letters* **2012**, *11*, 152–155.
33. Li, C.; Mo, L.; Zhang, D. Review on UHF RFID localization methods. *IEEE Journal of Radio Frequency Identification* **2019**, *3*, 205–215.
34. Huiting, J.; Flisijn, H.; Kokkeler, A.B.; Smit, G.J. Exploiting phase measurements of EPC Gen2 RFID tags. 2013 IEEE International Conference on RFID-Technologies and Applications (RFID-TA). IEEE, 2013, pp. 1–6.
35. Pelka, M.; Bollmeyer, C.; Hellbrück, H. Accurate radio distance estimation by phase measurements with multiple frequencies. 2014 International Conference on Indoor Positioning and Indoor Navigation (IPIN). IEEE, 2014, pp. 142–151.
36. Nikitin, P.V.; Martinez, R.; Ramamurthy, S.; Leland, H.; Spiess, G.; Rao, K. Phase based spatial identification of UHF RFID tags. 2010 IEEE International Conference on RFID (IEEE RFID 2010). IEEE, 2010, pp. 102–109.
37. Povalac, A.; Sebesta, J. Phase difference of arrival distance estimation for RFID tags in frequency domain. 2011 IEEE International Conference on RFID-Technologies and Applications. IEEE, 2011, pp. 188–193.
38. Scherhäufl, M.; Pichler, M.; Stelzer, A. UHF RFID localization based on phase evaluation of passive tag arrays. *IEEE Transactions on Instrumentation and Measurement* **2014**, *64*, 913–922.
39. Buffi, A.; Nepa, P.; Cioni, R. SARFID on drone: Drone-based UHF-RFID tag localization. 2017 IEEE International Conference on RFID Technology & Application (RFID-TA). IEEE, 2017, pp. 40–44.
40. Buffi, A.; Motroni, A.; Nepa, P.; Tellini, B.; Cioni, R. A SAR-based measurement method for passive-tag positioning with a flying UHF-RFID reader. *IEEE Transactions on Instrumentation and Measurement* **2018**, *68*, 845–853.
41. Motroni, A.; Nepa, P.; Magnago, V.; Buffi, A.; Tellini, B.; Fontanelli, D.; Macii, D. SAR-based indoor localization of UHF-RFID tags via mobile robot. 2018 International Conference on Indoor Positioning and Indoor Navigation (IPIN). IEEE, 2018, pp. 1–8.
42. Bernardini, F.; Buffi, A.; Motroni, A.; Nepa, P.; Tellini, B.; Tripicchio, P.; Unetti, M. Particle swarm optimization in SAR-based method enabling real-time 3D positioning of UHF-RFID tags. *IEEE Journal of Radio Frequency Identification* **2020**, *4*, 300–313.
43. Gareis, M.; Fenske, P.; Carlowitz, C.; Vossiek, M. Particle filter-based SAR approach and trajectory optimization for real-time 3D UHF-RFID tag localization. 2020 IEEE International Conference on RFID (RFID). IEEE, 2020, pp. 1–8.
44. G., M. La transfluence Durance-Isère Essai de synthèse du Quaternaire du bassin du Drac'(Alpes françaises). *Géologie Alpine* **1973**, *49*, 57–118.
45. Jongmans, D.; Bièvre, G.; Renalier, F.; Schwartz, S.; Beaurez, N.; Orengo, Y. Geophysical investigation of a large landslide in glaciolacustrine clays in the Trièves area (French Alps). *Engineering geology* **2009**, *109*, 45–56.
46. Fiolleau, S.; Borgniet, L.; Jongmans, D.; Bièvre, G.; Chambon, G. Using UAV's imagery and LiDAR to accurately monitor Harmalière (France) landslide evolution. Geophysical Research Abstracts, 2019, Vol. 21.
47. Fiolleau, S.; Jongmans, D.; Bièvre, G.; Chambon, G.; Lacroix, P.; Helmstetter, A.; Wathelet, M.; Demierre, M. Multi-method investigation of mass transfer mechanisms in a retrogressive clayey landslide (Harmalière, French Alps). *Landslides* **2021**, pp. 1–20.
48. Norrdine, A. An algebraic solution to the multilateration problem. Proceedings of the 15th international conference on indoor positioning and indoor navigation, Sydney, Australia, 2012, Vol. 1315.
49. Conn, A.R.; Gould, N.I.; Toint, P.L. *Trust region methods*; SIAM, 2000.
50. Van Loan, C.F. Generalizing the singular value decomposition. *SIAM Journal on numerical Analysis* **1976**, *13*, 76–83.

51. Anton, H.; Rorres, C. *Elementary linear algebra: applications version*; John Wiley & Sons, 2013.
52. Golub, G.; Kahan, W. Calculating the singular values and pseudo-inverse of a matrix. *Journal of the Society for Industrial and Applied Mathematics, Series B: Numerical Analysis* **1965**, *2*, 205–224.
53. Wang, G.; Qian, C.; Cui, K.; Shi, X.; Ding, H.; Xi, W.; Zhao, J.; Han, J. A Universal Method to Combat Multipaths for RFID Sensing. IEEE INFOCOM 2020-IEEE Conference on Computer Communications. IEEE, 2020, pp. 277–286.
54. Faseth, T.; Winkler, M.; Arthaber, H.; Magerl, G. The influence of multipath propagation on phase-based narrowband positioning principles in UHF RFID. 2011 IEEE-APS Topical Conference on Antennas and Propagation in Wireless Communications. IEEE, 2011, pp. 1144–1147.
55. Rembold, B. Optimum modulation efficiency and sideband backscatter power response of RFID-tags. *Frequenz* **2009**, *63*, 9–13.
56. ITU, R. Electrical Characteristics of the Surface of the Earth. *ITU-R P. 523-7* **1992**.
57. Lytle, R.J. Measurement of earth medium electrical characteristics: Techniques, results, and applications. *IEEE Transactions on Geoscience Electronics* **1974**, *12*, 81–101.
58. Azzouzi, S.; Cremer, M.; Dettmar, U.; Kronberger, R.; Knie, T. New measurement results for the localization of uhf rfid transponders using an angle of arrival (aoa) approach. 2011 IEEE International Conference on RFID. IEEE, 2011, pp. 91–97.
59. Sun, S.L.; Deng, Z.L. Multi-sensor optimal information fusion Kalman filter. *Automatica* **2004**, *40*, 1017–1023.
60. Sarkka, S.; Viikari, V.V.; Huusko, M.; Jaakkola, K. Phase-based UHF RFID tracking with nonlinear Kalman filtering and smoothing. *IEEE Sensors Journal* **2011**, *12*, 904–910.